8-1-2023

Ultrasonic study of water adsorbed in nanoporous glasses

Jason Ogbebor

John J. Valenza

Peter I. Ravikovitch

Ashoka Karunarathne

Giovanni Muraro

See next page for additional authors

Authors

Jason Ogbebor, John J. Valenza, Peter I. Ravikovitch, Ashoka Karunarathne, Giovanni Muraro, Maxim Lebedev, Boris Gurevich, Alexei F. Khalizov, and Gennady Y. Gor

Ultrasonic study of water adsorbed in nanoporous glasses

Jason Ogbebor [1], John J. Valenza,[2] Peter I. Ravikovitch,[2] Ashoka Karunarathne,[1] Giovanni Muraro,[2] Maxim Lebedev [3,4]
Boris Gurevich,[3] Alexei F. Khalizov [5,1] and Gennady Y. Gor [1,*]

[1]*Otto H. York Department of Chemical and Materials Engineering, New Jersey Institute of Technology, 323 Dr. Martin Luther King Jr. Boulevard, Newark, New Jersey 07102, USA*

[2]*Research Division, ExxonMobil Technology and Engineering Co., 1545 Route 22 East, Annandale, New Jersey 08801, USA*

[3]*Center for Exploration Geophysics, Curtin University, 26 Dick Perry Avenue, Kensington, Western Australia 6151, Australia*

[4]*Centre for Sustainable Energy and Resources, Edith Cowan University, 270 Joondalup Drive, Joondalup, Western Australia 6027, Australia*

[5]*Department of Chemistry and Environmental Science, New Jersey Institute of Technology, 323 Dr. Martin Luther King Jr. Boulevard, Newark, New Jersey 07102, USA*

Thermodynamic properties of fluids confined in nanopores differ from those observed in the bulk. To investigate the effect of nanoconfinement on water compressibility, we perform water sorption experiments on two nanoporous glass samples while concomitantly measuring the speed of longitudinal and shear ultrasonic waves in these samples. These measurements yield the longitudinal and shear moduli of the water-laden nanoporous glass as a function of relative humidity that we utilize in the Gassmann theory to infer the bulk modulus of the confined water. This analysis shows that the bulk modulus (inverse of compressibility) of confined water is noticeably higher than that of the bulk water at the same temperature. Moreover, the modulus exhibits a linear dependence on the Laplace pressure. The results for water, which is a polar fluid, agree with previous experimental and numerical data reported for nonpolar fluids. This similarity suggests that irrespective of intermolecular forces, confined fluids are stiffer than bulk fluids. Accounting for fluid stiffening in nanopores may be important for accurate interpretation of wave propagation measurements in fluid-filled nanoporous media, including in petrophysics, catalysis, and other applications, such as in porous materials characterization.

I. INTRODUCTION

Since the time of Lord Kelvin [1] and Derjaguin [2,3], numerous works have demonstrated that confinement affects fluid behavior, such as evaporation-condensation and freezing-melting phase transitions [4–6], transport properties [7,8], and derivative thermodynamic properties, such as the thermal expansion coefficient [9,10] and compressibility [11,12].

Over the past two decades an additional motivation for studying confined fluids emerged from the shale revolution. Extended reach horizontal drilling and hydraulic fracturing unlocked the potential of unconventional oil and gas assets commonly referred to as oil and gas shale. This industrial paradigm shift motivated interest in developing petrophysical techniques to characterize these assets. Conventional petrophysics is primarily concerned with mechanisms active on a length scale greater than 1 µm [13]. In contrast, unconventional oil and gas reservoirs primarily consist of oil and gas confined in nanoporous mudstones [14].

The seminal works of Gassmann [15] and Biot [16,17] showed how the elastic properties (compressibility or, the reciprocal property, bulk modulus) of a pore fluid contribute to the effective mechanical and elastodynamic response of a saturated porous medium. A number of petrophysical sonic logging techniques exploit this poromechanical response to infer the pore fluid properties. Elastic properties of a porous medium (be it dry or saturated with a fluid) can be inferred by measuring the speed of various stress waves. Utilizing several fluids, previous experimental studies explored the relationship between sound speed and relative saturation of nanoporous media [18,19]. All previous work indicates that fluids confined to nanopores exhibit elastic properties that deviate from those in the bulk [11,20–26]. Recent density functional theory calculations [27,28] and molecular simulations [29–31] confirm these observations.

While natural geological materials are of primary practical interest, these materials are characterized by a great deal of complexity such as a broad pore-size distribution and the presence of multiple components with disparate chemical makeup. To understand how confinement affects the elasticity of the fluid, it is more convenient to use a simpler porous medium with a single solid phase and a microstructure characterized by a large surface area and narrow pore-size distribution. Since we use sound to probe the mechanical properties, it is also preferable to work with a monolithic porous sample as opposed to granular media, which are known to exhibit large sound speed variations as a function of sample preparation (e.g., leading to different packing densities

*gor@njit.edu

between samples or even inhomogeneities within the same sample). Vycor glass is a suitable model nanoporous medium that adheres to the constraints listed above, and the solid skeleton is silica, a primary component in many rocks, including mudstones. Moreover, Vycor has been utilized in the adsorption-ultrasonic studies mentioned above, focused on confined liquid nitrogen [20,26], argon [11,22,24,25], and linear alkanes [21,23]. In addition, there are numerous experiments concerned with water confined in Vycor glass that explored adsorption-induced deformation [32,33], freezing [34,35], imbibition [36–38], the temperature of maximum density [39], and the structure and fluid dynamics of water in the pores [40–43]. Note that Murphy [44] carried out an adsorption-acoustic study of water in Vycor glass but focused on the attenuation of low-frequency acoustic waves and did not probe the elasticity of water in the pores. Cucini *et al.* also studied sound propagation in water-saturated Vycor glass, focusing on the dynamics of water in nanopores but not the elasticity [45]. Experiments focusing on the effect of nanoporous confinement on the compressibility of water via adsorption-acoustic methods are lacking. Here we present an experimental study of water vapor adsorption on nanoporous glass samples accompanied with *in situ* ultrasonic measurements, probing the elasticity of water-laden porous glass. Contrary to similar previous experimental works [11,20–22,24–26] that utilized nonpolar fluids, water is polar so it may interact differently with the glass surface. Furthermore, water is a substance ubiquitous in nature and is relevant to the geological context discussed previously.

We perform water sorption experiments on two nanoporous glass samples while concomitantly measuring the speed of longitudinal and shear ultrasonic waves in these samples. This includes both the adsorption and desorption branches of the isotherm. Using these measurements, we calculate the longitudinal and shear moduli of the samples as a function of relative humidity (RH). These moduli are then used to compute the bulk modulus, which shows a sharp increase for both samples when the pores become completely filled with the liquid water. These elevated bulk moduli of fully saturated samples are then used to infer the bulk modulus of the confined water using the Gassmann theory. Our observations also show a significant hysteresis effect, in which the moduli remain elevated until capillary evaporation of the pore fluid occurs. The bulk modulus of confined water estimated with the Gassmann model is higher than the modulus of the bulk water obtained from an equation of state. Our observations are consistent with previous experimental and computational studies on nonpolar liquids, suggesting that confinement enhances the liquid modulus irrespective of molecular characteristics like polarizability.

II. METHODS

In general, our approach consists of measuring the speed of stress waves through a nanoporous medium as the pores is gradually filled with liquid water. The water saturation is controlled by varying the relative humidity around the two nanoporous samples. Since we cannot measure the time of flight and weight of the sample at the same time, after the RH equilibrates, the time of flight is recorded on one sample

TABLE I. Physical properties of samples V (Vycor glass) and C (controlled-pore glass).

Property	Sample V	Sample C
dry mass (g)	1.1363 ± 0.0001	1.6161 ± 0.0001
porosity ϕ	0.330 ± 0.001	0.332 ± 0.001
apparent density (g/cm^3)	1.412 ± 0.009	1.486 ± 0.009
solid density (g/cm^3)	2.108 ± 0.007	2.247 ± 0.008
mean pore diameter (nm)	7.5	7.2
specific surface area (m^2/g)	145	158
specific pore volume (cm^3/g)	0.220	0.225

and the other sample is weighed; then the RH is adjusted to a new value. These steps are repeated until both the adsorption and desorption isotherms are complete. Then the samples are swapped and the entire set of measurements is repeated. A schematic of the adsorption-ultrasound system is shown in Fig. 1 and the measurements are described in greater detail below.

A. Porous glass

This study is conducted on two nanoporous glass rods of similar composition and pore structures, which will be referred to as samples V and C. Sample V is Corning Vycor glass (No. 7930) with diameter $d_V = 0.635$ cm and length $L_V = 2.540$ cm. Vycor is an optically transparent porous glass, which is mostly silica. Its structure is comprised of wormlike channel pores with a mean diameter of 7–8 nm. Due to its accessible and well-defined pore space, optical transparency, and ability to be manufactured in a variety of shapes, Vycor has been utilized as a model porous medium for studying the physics of confined phases for several decades [11,20,21,24,26,32,35–37,41–44]. Sample C is a controlled-pore glass with diameter $d_C = 0.622$ cm and length $L_C = 3.544$ cm. The physical properties of both samples are listed in Table I. All dimensional measurements have an uncertainty of ± 0.002 cm. The apparent density is the mass of the dry sample divided by the measured volume, which includes pore volume. The solid density is calculated as the dry mass divided by the solid volume [measured volume multiplied by $(1 - \phi)$].

Both samples are characterized by nitrogen adsorption porosimetry to determine the porosity and pore-size distributions. Adsorption isotherms of nitrogen at 77 K are measured with the volumetric adsorption instrument Autosorb-1C (Anton Paar). The samples are outgassed using a turbomolecular pump to residual pressure below 7.5×10^{-4} torr at $300\,^\circ$C for 16 h prior to running the isotherms. The entire monolithic glass rod (with mass exceeding 1 g in both cases) is used for the measurements. Due to the large size, the measurements take four days, over which the Dewar is carefully refilled with nitrogen when the pressure is greater than that corresponding to capillary condensation. The pore-size distribution (PSD) is calculated using the nonlocal density functional theory model for cylindrical pores. The adsorption branch is used to determine the PSD along with the model for metastable adsorption, as in Ref. [46]. The PSD of Vycor glass is in good agreement with previously reported measurements [47].

The samples used in this study are exposed to ambient air before and during the experiments detailed herein. At
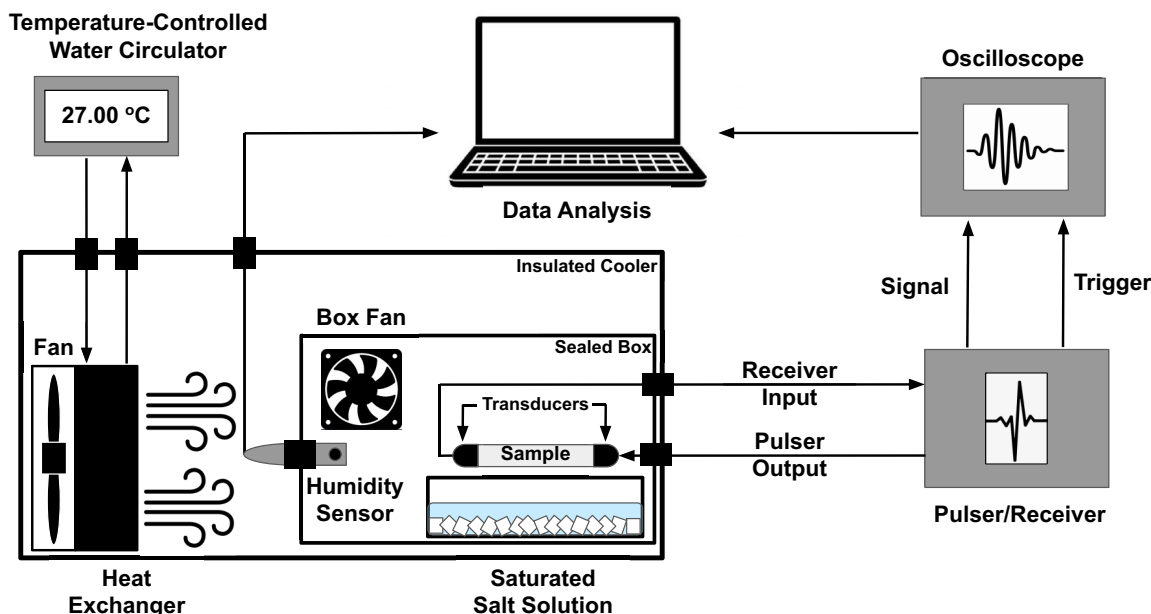
FIG. 1. Schematic of the adsorption-ultrasound system. The cables for the transducers, humidity sensor, and box fan are fed into the chamber using sealed feedthroughs. Thermal insulation is applied to seal the holes through which cables and tubes passed through the walls of the cooler.

the end of adsorption-ultrasonic experiments the samples are vacuumed and heated. As a result of heating, the samples become yellow in color (Fig. 12). The color is likely caused by products of thermal decomposition of trace organic molecules adsorbed from air.

B. Humidity control

Water sorption experiments are carried out in humid air. The RH, equal to p/p_0, is the ratio of the partial vapor pressure p to the saturation vapor pressure of water p_0. The RH is controlled by placing various salt solutions (following Yurikov *et al.* [48]) in a hermetically sealed 2.5-l anaerobic box (AnaeroPack™ rectangular jar, Thermo Scientific™ R681001). Each solution contains enough excess salt to yield precipitate, so the water activity remains constant. A list of salt solutions and the corresponding RH at room temperature is shown in Table II. We add multiple wire feedthroughs to the box that permits continuous monitoring of the relative humidity in the chamber using a Vernier™ sensor with accuracy of ±2% RH, a resolution of 0.01% RH, and a response time (time for a 90% change in reading) of approximately 40 s in well-mixed air. A 40-mm, 12-V dc box fan continuously mixes the air in the box. Finally, the box is placed in a Coleman 48-qt beverage cooler equipped with a finned shell-and-tube heat exchanger and a 120-mm 24-V dc box fan. Temperature-controlled water is pumped through the heat exchanger by a Fisherbrand™ Isotemp™ bath circulator, model 6200 R20, with the temperature set to 27.00 °C ± 0.025 °C.

C. Ultrasonic measurements

The sample is held between two transducers, using 0.172-mm-thick nitrile rubber as a couplant, with a custom-built

clamp assembly. The assembly contains three springs to press the transducers against the ends of the sample (see Appendix, Fig. 12). We use longitudinal and transverse contact transducer pairs (Olympus, parts V1091 and V157-RM, respectively) with a fundamental frequency of 5 MHz and a diameter of 6.35 mm. The source transducer is connected to a pulser/receiver (JSR Ultrasonics brand DPR300), which generates negative spike pulses 10–70 ns in duration. The receiving transducer is used to record the transmitted signal. The pulse repetition rate is set to 100 pulses per second at 100–250 V output. The pulser simultaneously sends a square wave trigger to the oscilloscope (Tektronix DPO2000B, 200 MHz, 1 GS/s, 1 Mpts record length) used to monitor the receiving transducer. Once the oscilloscope is triggered, defining $t = 0$,

TABLE II. Desiccant salts used in this work and their expected relative humidities at $T = 27$ °C [49].

Salt name	Formula	RH (%)
lithium chloride	$LiCl$	12
potassium acetate[a]	$KC_2H_3O_2$	24
calcium chloride	$CaCl_2$	30
potassium carbonate	K_2CO_3	45
magnesium nitrate	$Mg(NO_3)_2$	53
sodium bromide	$NaBr$	58
sodium chlorate	$NaClO_3$	75
sodium chloride	$NaCl$	77
ammonium sulfate	$(NH_4)_2SO_4$	81
potassium bromide	KBr	84
potassium bisulfate	$KHSO_4$	86
potassium chloride	KCl	88
sodium sulfate	Na_2SO_4	93
potassium sulfate	K_2SO_4	98

[a]The data for potassium acetate are not included in the results; they are addressed in the Appendix.
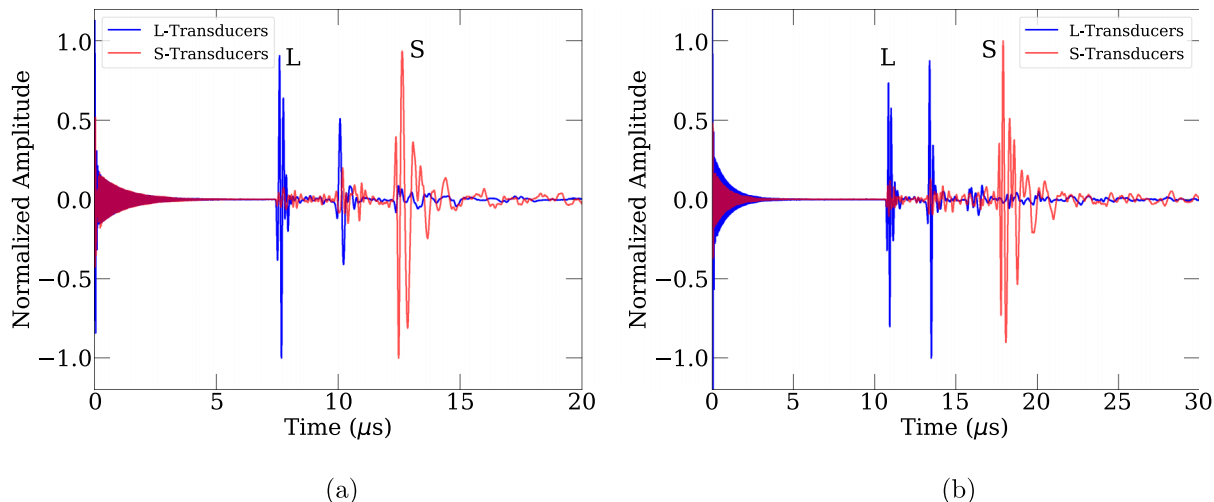
FIG. 2. Comparison of waveforms produced by longitudinal and shear transducers through (a) sample V and (b) sample C at ambient conditions (approximately 30% RH), with the waveform of interest labeled L or S for longitudinal and shear, respectively: Blue (darker), generated and recorded by longitudinal transducers, and red (lighter), generated and recorded by shear transducers.

the transmitted waveform is logged at a rate of 250 MHz. The oscilloscope is set to trigger at an amplitude of 1.4 V on the rising edge of the square trigger wave. The exact triggering amplitude has no effect on the time of flight. A single measurement consists of averaging 512 transmitted waveforms to improve the signal-to-noise ratio.

D. Gravimetric measurements

While the ultrasonic measurements are performed on a sample clamped between the transducers, the mass of the companion sample is concurrently monitored to determine the mass of water adsorbed. The companion sample sits on a watch glass adjacent to the mounted sample. After the relative humidity is stabilized and the time of flight is measured, the box is opened momentarily to remove the companion sample for weighing. The mass is measured on a Mettler AT261 DeltaRange analytical balance (weighing capacity 205 g), with a linearity of ±0.15 mg. The time necessary to accurately measure the mass (seconds) is very short relative to the characteristic time for water vapor equilibration within the sample (hours). Initially, water uptake in sample C is monitored while measuring the sound speeds on sample V. After completing the adsorption and desorption branches, the samples are swapped and the experiments are repeated to obtain a complete data set.

E. Data analysis

Typical waveforms recorded in this study are given in Fig. 2, which shows the signals produced by longitudinal and shear transducers. The time of flight is determined using a standard cross-correlation technique where the transmitted waves are correlated with a reference waveform. The latter is given by measuring the signal across two transducers clamped together but separated by the nitrile couplant. Figure 3 shows a comparison of the waveform measured through a porous glass sample and the waveform observed with the transducers clamped together after, which is shifted to maximize the

correlation coefficient. The vertical dashed line indicates the time of flight determined from the cross correlation. The cross correlations are performed using the PYTHON library SCIPY.SIGNAL.CORRELATE, which follows a standard approach used in signal processing [50]. The wave features between the longitudinal and shear waves seen in Fig. 2 appear for samples which are smaller in diameter than the transducers, which is the case for both samples considered here. This is additionally confirmed by performing the measurements on nonporous borosilicate glass samples of different diameters and lengths.
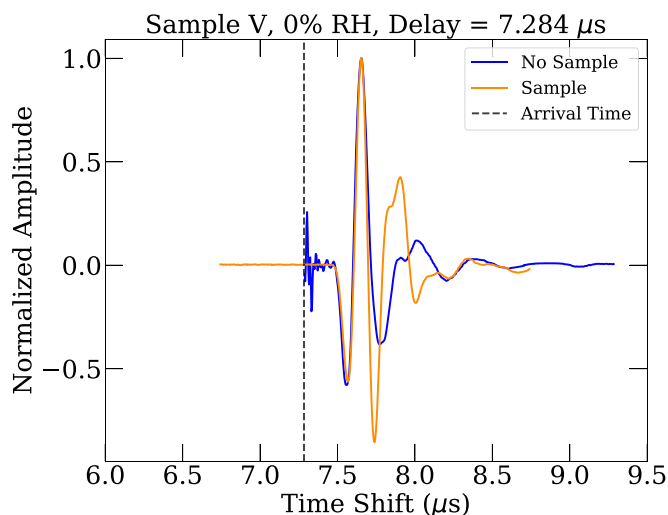
FIG. 3. Visual representation of the cross-correlation method, in which a reference waveform [blue (darker in grayscale) and with a longer tail] is shifted in the time domain to obtain the maximum similarity (correlation) between the two waveforms. The wave that travels through the sample is in red (lighter in grayscale). The time shift that produces the maximum correlation coefficient represents the travel time used for calculating sound velocity. The waveforms depicted in the figure are longitudinal waves produced by longitudinal transducers.

Another method to determine time of flight involves fitting the initial descent of the waveform to a linear function. The intersection of that line with the x axis is defined as the arrival time. The two methods differ by approximately 10 m/s, corresponding to less than 0.3%. For consistency, the results presented here rely on the cross-correlation method.

The time of flight for the independent longitudinal and shear arrival are used to determine the corresponding sound speed given the sample length (v_L and v_S, respectively). The sound speed is then combined with the sample density ρ to determine the longitudinal and shear moduli (M and G, respectively):

$$M = \rho v_L^2, \quad G = \rho v_S^2. \tag{1}$$

These moduli are then used to calculate the bulk modulus K by the relation

$$K = M - \tfrac{4}{3}G. \tag{2}$$

This quantity represents the bulk modulus of the composite (nanoporous glass plus adsorbed water). When the pores are completely filled with fluid, K can be related to the bulk moduli of the constituents by the Gassmann equation [15,30]

$$K = K_0 + \frac{\left(1 - \frac{K_0}{K_s}\right)^2}{\frac{\phi}{K_f} + \frac{1-\phi}{K_s} - \frac{K_0}{K_s^2}}, \tag{3}$$

where ϕ is the sample porosity, K is the bulk modulus, and the subscripts 0, s, and f correspond to the dry porous body, the solid phase, and the pore fluid, respectively. It is convenient to rearrange Eq. (3) to solve for the quantity of interest, the bulk modulus of the confined fluid:

$$K_f = \phi(K - K_0)$$

$$\times \left[\left(1 - \frac{K_0}{K_s}\right)^2 - \frac{(1-\phi)(K-K_0)}{K_s} + \frac{K_0(K-K_0)}{K_s^2} \right]^{-1}. \tag{4}$$

The parameter K_s is estimated using the modified Kuster and Toksöz (KT) effective medium theory [51–53], which gives K_s and G_s when K_0, G_0, and ϕ are known. A summary of the KT theory used to determine K_s is in the Appendix. This theory is written for cylindrical pores, which is a reasonable approximation of the wormlike pores in the samples studied in this work.

To measure the dry elastic properties, both samples are outgassed at approximately 10^{-5} torr for 24 h before being transferred to a glove bag purged of ambient air and refilled with nitrogen. The ultrasound speed is measured using a combination of longitudinal and shear transducers, after which the samples are removed from the bag to measure their mass. Following these measurements, to drive off chemically adsorbed water from the pore surface, the samples are heated to 200 °C at approximately 10^{-5} torr. At these conditions, the samples are allowed to outgas for 24 h before cooling to room temperature. Ultrasonic and gravimetric measurements are then taken in the same manner as described above.

Following the aforementioned measurements, the samples are washed in a 30% solution of hydrogen peroxide at 80 °C to oxidize and remove trace organics from the pore surface.
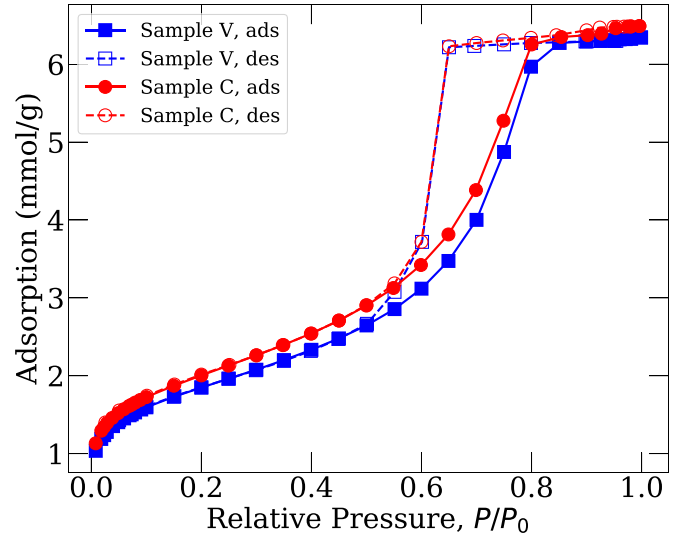

FIG. 4. Nitrogen adsorption isotherms on samples V and C measured at 77 K using a Autosorb-1C automated gas sorption system (Anton Paar). Closed markers represent adsorption and open markers represent desorption.

During washing, the samples lose their yellow tint and become clear. The samples are then transferred into deionized water to remove the peroxide solution. The above-described vacuum measurements are repeated on the cleaned samples. We note here that the elastic properties of Vycor glass are sensitive to temperature. In particular, Scherer [54] has shown that heat can irreversibly stiffen nanoporous glass. For this reason, we estimate the fluid bulk modulus using the dry mechanical properties obtained from the vacuum measurements described above, before the first heating cycle. The results of later measurements are provided in the Appendix.

III. RESULTS

A. Nitrogen gas adsorption

The nitrogen adsorption isotherms are shown in Fig. 4, which indicates the responses are nearly indistinguishable between the samples. Prior to the capillary condensation, sample C adsorbs slightly more nitrogen than sample V, whereas the plateaus and the capillary evaporation regions are practically identical for the two samples. Abrupt and nearly complete capillary evaporation occurs at the same relative pressure of $p/p_0 \sim 0.6$, indicating that access to the porosity occurs through pores of a similar size. Figure 5 shows the pore-size distribution determined from the adsorption branch of the isotherm. Again, the pore-size distributions of the samples are very similar, with the small difference observed near the tail corresponding to the largest pore diameters.

B. Water adsorption isotherms

The relative mass of adsorbed water and saturation determined from the gravimetric measurements are shown in Figs. 6(a) and 6(b). Saturation is estimated as $s = \Delta m / \Delta m_{98}$, where Δm is the change in sample mass at a given relative humidity and Δm_{98} is the change in sample mass at RH 98%.
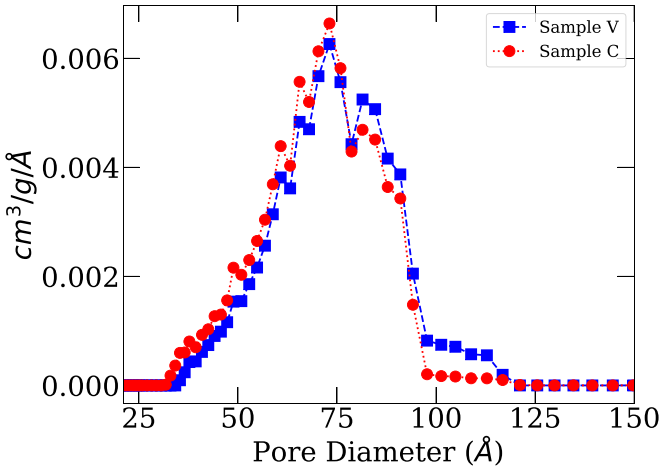
FIG. 5. Pore-size distribution calculated from the nitrogen adsorption isotherms in Fig. 4 for samples V and C. The differential distribution is a measure of the contribution of each pore size to the total pore volume per gram of each sample.

Since the mass uptake is largely complete above RH equal to 0.9, s is a measure of the relative pore volume filled with water.

The isotherms are type IV, in agreement with the well-established adsorption data for water in Vycor glass [32,55]. Vertical error bars represent the precision of the dry mass of both samples and of the balance used to measure the mass at subsequent relative pressures. The point at the origin is not measured, but it is reasonable to assume there is no adsorbed fluid at a relative pressure of zero. As humidity rises, the amount of water adsorbed gradually increases. In the region below the knee in the curve (e.g., $p/p_0 \leqslant 0.2$), a monolayer of water forms on the internal surface. Capillary condensation begins near a relative pressure of 0.75, where the water bridges the gap between the pore walls and fills the pores.

C. Longitudinal and shear wave speeds

The longitudinal and shear wave speeds are shown in Figs. 6(c) and 6(d) for both samples (using the same vertical scale for both speeds). Each data point represents the average of up to ten time-of-flight measurements taken several hours after the RH stabilizes. As previously indicated, the speeds are determined from time of flight by cross correlation with the waveform measured with no sample. The time of flight varies by no more than 0.1% over several hours after the RH stabilizes. The error bars account for this variation and the error associated with measuring the sample length. In most cases the range of the error is smaller than the markers on the plot.

Both samples exhibit similar behavior with respect to sound propagation throughout the adsorption and desorption processes. As RH increases, the sound speeds (both longitudinal and shear) gradually decrease, followed by a steeper decline with the onset of capillary condensation. The minimum in v_L is observed around $p/p_0 = 0.85$, where the adsorbed fluid almost completely fills the pores. For longitudinal waves, this is followed by a marked increase in speed. In contrast, v_S levels off and continues gradually decreas-

ing as maximum saturation is reached. At the beginning of desorption, v_L gradually decreases while v_S increases, following the same slope observed during the end of adsorption. As the hysteresis in mass adsorption closes, both speeds rise back toward the values observed at the lowest relative humidity. The increase in v_S is more dramatic than in v_L, resembling the hysteresis loop observed in the adsorption isotherms.

The longitudinal and shear wave speeds in sample C exhibit a hysteresis gap (approximately 30 m/s and approximately 20 m/s, respectively) that remains open below $p/p_0 = 0.6$. To ensure that this is not an artifact of the cross-correlation technique (e.g., caused by a difference in the shape of the waveforms), the sound speed is also determined by comparing only the initial descent of each waveform. With this method, the difference between adsorption and desorption decreases but remains noticeable (approximately 20 m/s). We note that prior to the experimental results presented in this work, sample V was used for initial adsorption and ultrasonic testing. During these tests, sample V was exposed to humidity swings between 12% and 98%. It is plausible that sample V had already undergone its adsorption-induced hysteresis.

D. Elastic moduli

Figures 6(e) and 6(f) show the longitudinal and shear moduli of both samples using the same vertical scale for both moduli. The moduli are calculated using Eq. (1), where we account for changes in sample density associated with water vapor sorption. In contrast to observations concerning the sorption of hexane [21] and argon [24] in Vycor, the longitudinal modulus M of the glass sample with water slightly increases at low relative pressures. The increase levels off near $p/p_0 \approx 0.6$, followed by a decrease until $p/p_0 \approx 0.85$. After capillary condensation, M increases sharply, mimicking v_L. On desorption, M remains elevated until the sorption hysteresis loop closes, indicating evaporation of the pore fluid. This is the case for longitudinal modulus of both samples. In contrast, the shear modulus G remains constant throughout the vapor sorption cycle. The bulk modulus K, calculated from Eq. (2) and shown in Fig. 7, exhibits similar behavior for both samples.

The values of K observed while water fully occupies the pore volume (RH greater than 0.85 during the adsorption and RH greater than 0.75 during desorption) are used to calculate the isothermal bulk modulus of confined liquid water using Eq. (4). The resulting fluid bulk modulus is shown in Fig. 8. We refer to this quantity as isothermal but note that the heat capacity ratio of liquid water at 1 atm and 300 K is 1.012 [56], making the difference between isothermal and adiabatic bulk modulus negligible. Previous studies [11,12,21] reported a linear relation between a fluid's bulk modulus and the Laplace pressure P_L,

$$P_L = \frac{R_g T}{V_m} \ln \left(\frac{p}{p_0} \right), \tag{5}$$

where R_g is the ideal gas constant, T is the absolute temperature, and V_m is the molar volume of the fluid. Figure 8 shows the values of K_f determined in this work along with the
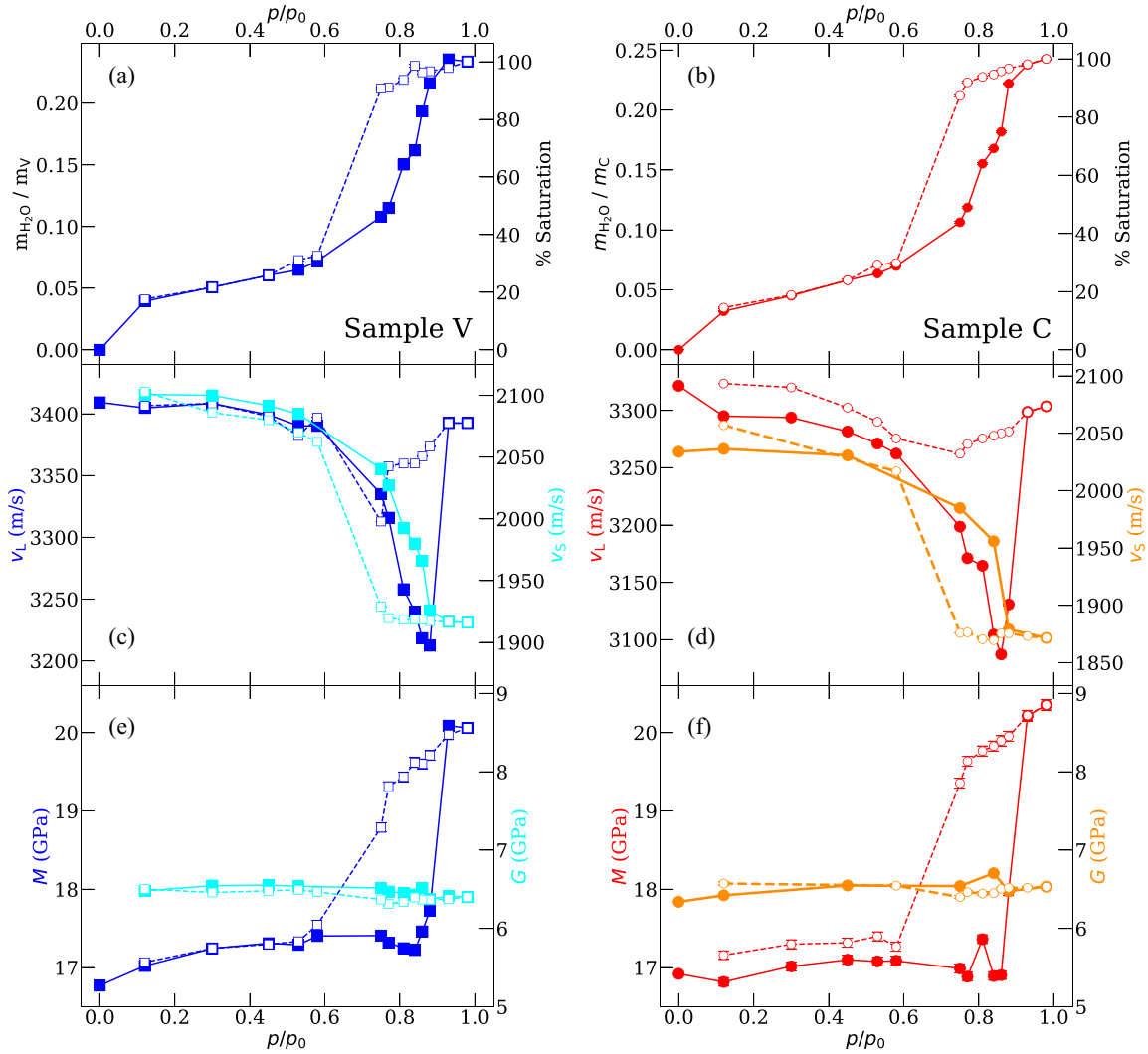
FIG. 6. Results of ultrasonic and gravimetric measurements during adsorption (closed markers and solid lines) and desorption (open markers and dashed lines). Lines connect adjacent data points as a guide to the eye. Sample V is represented in blue (left column) and sample C in red (right column). Longitudinal speed and modulus share the same shade as the adsorption isotherms. Shear speed and modulus use lighter shading (cyan for sample V and orange for sample C). In grayscale these lighter shades appear gray. (a) and (b) Water adsorption isotherms, mass of water adsorbed m_{H_2O} relative to the dry mass of each sample m_V and m_C. (c) and (d) Longitudinal v_L and shear v_S wave speeds. (e) and (f) Longitudinal and shear moduli calculated by Eq. (1). The speed and moduli presented at $p/p_0 = 0$ were obtained from the vacuum measurements explained in Sec. II.

isothermal bulk modulus of water in the bulk as a function of P_L or the bulk pressure, respectively. The K_f is calculated from Eq. (4) using the values of K_0 and K_s listed in Table III. The isothermal bulk modulus data for liquid water at 27 °C is calculated using the COOLPROP PYTHON library [56], which utilizes the equation of state by Wagner and Pruß [57]. It is worth noting that at relative pressures below 1.0, P_L is negative, indicating the confined water is under suction. The data corresponding to positive pressure represent the isothermal bulk modulus of bulk water.

IV. DISCUSSION

A. Comparison of water adsorption isotherms

Figure 9 includes data from previous works concerning water adsorption in Vycor. Overall, there is fairly good agreement along the adsorption branches. While Amberg and

McIntosh observed a smaller hysteresis loop during desorption, we are unable to reproduce this in our samples due to the lack of an appropriate desiccant between 58% and 75% RH. Furthermore, we observe good agreement between samples V and C, reflecting their similar composition and pore-size distribution.

B. Applicability of the Gassmann theory

The Gassmann equation, which is used here to relate the measured modulus of the solid-fluid composite to the moduli of constituents, was originally derived for quasistatic deformations (e.g., the elastic properties must be probed by small perturbations). Therefore, we must consider the relevance of this theory to moduli inferred from the transmission of ultrasound. One constraint in the Gassmann theory is that the average pore radius must be much smaller than the viscous
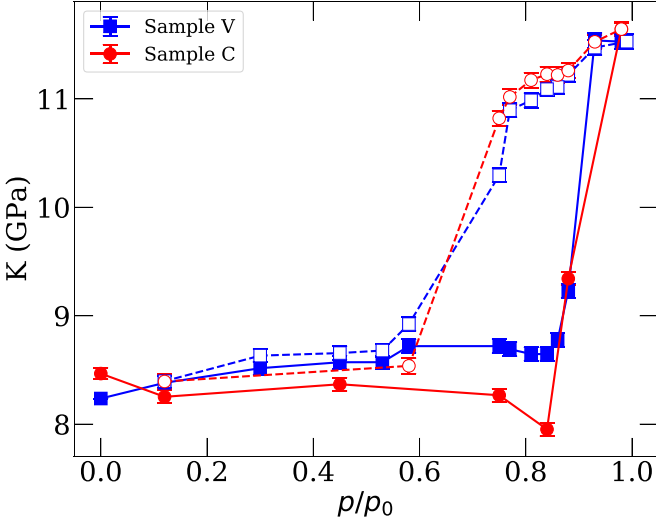
FIG. 7. Bulk modulus of samples V and C calculated by Eq. (2). Closed markers represent data on the adsorption branch, while open markers represent desorption. The error bars are propagated from the uncertainty in the longitudinal and shear moduli.

skin depth of the fluid $\delta = \sqrt{\eta / \pi f \rho_f}$, where η and ρ_f are the dynamic viscosity and density of the pore fluid, respectively, and f is the frequency of the propagating wave. The transducers used in this work have a nominal frequency of 5 MHz. We estimate the density of water in the pores at 100% saturation as $\rho_f \approx 1044$ kg/m^3. Assuming the dynamic viscosity of liquid water $\eta = 8.509 \times 10^{-4}$ Pa s at 27 °C is unaffected by confinement, the viscous skin depth can be estimated as $\delta = 228$ nm. For a more conservative estimate, we consider the maximum exhibited frequency of the transducers, 10 MHz, resulting in a viscous skin depth of $\delta = 161$ nm. The
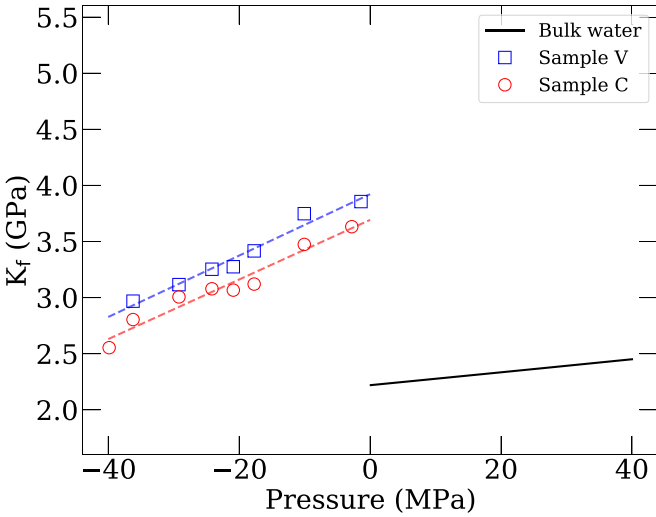

FIG. 8. Bulk modulus of water in Vycor glass calculated from the data in Fig. 7 using Eq. (4) plotted as a function of Laplace pressure (5). The solid line represents the modulus of bulk water as a function of bulk pressure calculated based on Ref. [57]. The dashed lines through the data markers are linear fits. The negative part of the *x* axis represents the Laplace pressure P_L, while the positive part of the *x* axis represents bulk fluid pressure.
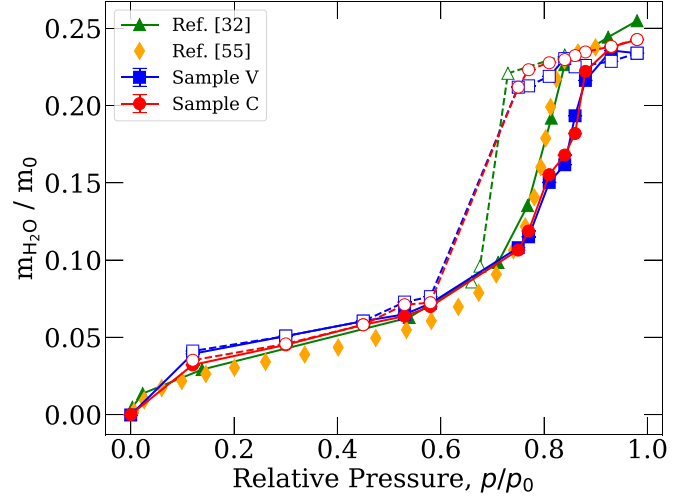

FIG. 9. Adsorption isotherms of water on nanoporous Vycor glass from two literature sources: By Amberg and McIntosh [32] at 25.8 °C and by Markova *et al.* [55] at 25 °C, compared with the isotherms measured in this work at 27 °C. Adsorption is represented by closed markers and desorption by open markers. The data from Markova *et al.* do not include desorption. Lines connecting markers are drawn to guide the eye.

pores in either sample are 7 nm, which is at least an order of magnitude smaller than the minimum viscous skin depth δ.

Another stipulation of the Gassmann theory is that the constituent fluid has a shear modulus of zero, so the shear modulus of the composite is not affected by fluid adsorption. In our case, the shear moduli of both samples are constant throughout sorption cycle. The Gassmann theory also requires the frequency to be sufficiently low for the fluid pressure to equilibrate throughout the pore space within one wave period. This requires that the frequency be much lower than the characteristic frequency of the squirt-flow relaxation, which is on the order of $f_c = \varrho^3 K_f / \eta$, where ϱ is the (smallest) pore aspect ratio in the system (see, e.g., [59], Chap. 6). For frequencies higher than f_c, the shear modulus of the fully saturated sample should be significantly higher than for the dry sample [59,60]. The fact that our measurements (as well as ultrasonic measurements on Vycor during adsorption of nitrogen [20] and argon [11]) show a constant shear modulus in the entire range of liquid saturation from 0 to 100% confirms that Vycor has no pores with very small aspect ratios (cracks). Finally, we note that the Gassmann theory requires that the wavelength of the probing ultrasound be much smaller than the diameter of the porous sample. In our experiments, the wavelength never exceeds 0.7 mm, which is more than nine times smaller than the diameter of either sample.

C. Comparison of samples V and C

The water adsorption isotherms in Fig. 6 are plotted as the mass of water adsorbed divided by the dry mass of each sample so that the isotherms can be objectively compared. The samples exhibit close agreement until the end of capillary condensation on the adsorption branch ($p/p_0 \approx 0.85$), after which the relative mass adsorbed in sample C is greater than that observed in sample V. On the desorption branch, this

TABLE III. Calculated mechanical properties of samples V and C from ultrasound speed measurements after outgassing at 10^{-5} torr for 24 h without heating. Other sets of values for Vycor 7930 are reported by Scherer [54] via sonic resonance, Vichit-Vadakan and Scherer [58] via beam bending, and Schappert and Pelster [11] via a pulse-echo ultrasound method. Here M_0, G_0, K_0, and v_0 are the longitudinal, shear, and bulk moduli and Poisson's ratio, respectively, of the dry porous material. The K_s is calculated using the modified Kuster-Toksöz theory outlined in the Appendix.

Source	M_0 (GPa)	G_0 (GPa)	K_0 (GPa)	v_0	K_s (GPa)
sample V	16.77 ± 0.06	6.40 ± 0.02	8.24 ± 0.06	0.192 ± 0.002	18.12
sample C	16.92 ± 0.06	6.34 ± 0.03	8.46 ± 0.06	0.200 ± 0.003	19.13
sonic resonance	15.64[a]	6.34	7.19[a]	0.15	15.37
beam bending	15.9	6.08	7.8	0.16	14.3
pulse echo	16.88	6.86	7.73	0.23	10.48

[a]Scherer reports the Young's modulus E of his porous sample. Along with his reported shear modulus and Poisson's ratio, it is possible to calculate the longitudinal and bulk moduli.

difference persists until the beginning of capillary evaporation ($p/p_0 \approx 0.75$), where the hysteresis loop begins to close.

Qualitative agreement between the samples is also observed for the sound speeds and the inferred moduli. Subtle quantitative differences can be attributed to the initial properties of both samples. For instance, the longitudinal and shear moduli are similar, but v_L and v_S differ between each sample by more than 100 m/s due to the samples having different solid densities (see Table I).

D. Mechanical properties of dry samples and confined water

In Table III the calculated mechanical properties of samples V and C are presented alongside those reported by Scherer for the same material via sonic resonance [54], by Vichit-Vadakan and Scherer using a beam-bending method [58], and by Schappert and Pelster using pulse-echo ultrasound measurements [11]. While the shear modulus of both samples agrees with the literature sources, we observe longitudinal moduli higher than any of the listed values. This leads to higher values for K_0 and K_s. Table III also shows the Poisson ratio v_0 of the dry samples

$$v_0 = \frac{M_0 - 2G_0}{2M_0 - 2G_0}. \tag{6}$$

Note that the bulk modulus of the fluid from Eq. (4) is sensitive to the values of K_0 and K_s, where the latter is the main source of potential uncertainties. If the dry elastic constants reported by Scherer and Vichit-Vadakan and by Schappert and Pelster are used to calculate K_s of Vycor glass via the modified KT theory, K_f inferred from the Gassmann theory will differ from the results in Fig. 8, as discussed in Ref. [30]. We find that a hypothetical underestimate of K_s by 10% or 20% causes an overestimate of K_f by 20% and 50%, respectively.

Irrespective of the values for K_0 and K_s, the fluid bulk modulus is linearly dependent on the pressure of the fluid in the pores (represented here by the Laplace pressure for simplicity) [27,61], which is consistent with the Tait-Murnaghan equation [62,63]

$$K_f(P_L) \approx K_f(0) + \alpha P_L, \tag{7}$$

where $\alpha = dK_f/dP_L$. Previous molecular simulation studies suggested that α for argon or nitrogen in silica pores is similar to that for bulk liquid argon [29,64,65] or liquid nitrogen [31], respectively. However, Fig. 8 indicates that confined water exhibits a different α than that exhibited by bulk water ($\alpha = 5.76$), in particular, $\alpha \sim 25.6$ for sample V and $\alpha \sim 27.8$ for sample C. These deviations are too high to be explained by uncertainties in the modulus K_s used for calculation of K_f from the experimental data.

Molecular simulation parametric studies of confined argon showed that when the solid-fluid interactions are stronger, the parameter α increases [65]. It could be that confinement affects the parameter α for water differently than for simple fluids, such as nitrogen or argon. More insight into α of confined water can be obtained from experiments and simulations of water in nanopores of various compositions.

V. CONCLUSION

To investigate the compressibility of confined water, we performed water vapor sorption experiments on two nanoporous glass samples and concomitantly monitored the effect on longitudinal and shear sound speed. Using the measured density of the water-laden glass, we inferred the longitudinal and shear moduli as a function of relative humidity. The longitudinal modulus varied with relative humidity, while the shear modulus did not change. Therefore, we utilized the Gassmann theory to infer the bulk modulus of water confined in the saturated glass. For both of the porous samples, we found that the modulus of confined water is consistently greater than that of bulk liquid water at the same temperature. Furthermore, the modulus of the confined water exhibited a linear dependence on Laplace pressure. Altogether these observations are consistent with previously reported data on nonpolar fluids, such as nitrogen or argon, suggesting that confinement causes significant stiffening for any fluid. Note that the modulus increase reported here is more pronounced than that reported for the noted nonpolar fluids confined to the same nanoporous glass.

This work should assist with the progression towards borehole-based ultrasonic measurements to probe natural nanoporous media, such as shale and coal, in order to detect specific confined fluids. While we investigated the effects of confinement on one fluid found in subsurface reservoirs, additional work is necessary to yield a useful measurement technique. In particular, similar studies using other relevant fluids, like hydrocarbons or salt solutions, or nanoporous me-

TABLE IV. Calculated mechanical properties of sample V from ultrasound speed measurements after following the procedure outlined in the main text. The K_s is calculated using the modified Kuster-Toksöz theory outlined in the Appendix and K_f is calculated using Eq. (4), with the respective dry and solid moduli.

Sample condition	M_0 (GPa)	G_0 (GPa)	K_0 (GPa)	ν_0	K_s (GPa)	K_f (GPa)
12% RH	17.02	6.48	8.38	0.193	18.46	3.635
prewash, ambient	16.77	6.40	8.24	0.192	18.12	3.855
prewash, 200 °C	17.54	6.95	8.27	0.172	17.42	4.114
postwash, ambient	16.45	6.40	7.91	0.181	16.98	4.561
postwash, 200 °C	17.72	6.90	8.51	0.181	18.26	3.609

dia with a range of physical properties would aid in assessing the utility of ultrasound to excite a characteristic response.

The raw data for Figs. 4–9 and 11 are available in the Supplemental Material [66]. Each file is written in plain text (.txt) or comma-separated values (.csv), and named for each respective figure.

APPENDIX: ADDITIONAL EXPERIMENTAL DETAILS

1. Estimates of dry properties after vacuum outgassing

Tables IV and V show the results of ultrasound speed measurements to calculate the elastic properties of samples V and C after outgassing at a pressure of 10^{-5} torr, as outlined in Sec. II. The samples were first outgassed at room temperature and then at 200 °C. Since darkening of the samples was observed after heating, the samples were then washed and the above measurements were repeated. The tables also show the resultant bulk modulus of water from Eq. (4), using the corresponding dry and solid bulk moduli. The values obtained from the prewash, ambient (not heated, not washed) measurements are used for calculating K_f.

After the experiments presented in the main text, one of the shear ultrasonic transducers became inoperable. For this reason, the travel time of shear waves needed to be recorded using the pulse echo method. In sample V this proved difficult due to its shorter length and the presence of noise in the signal, but the travel time of both longitudinal and shear waves could be measured successfully in sample C. Further, during the second ambient vacuum cycle, sample V developed a fracture along the axial direction near the center of the sample. Attempts at ultrasonic measurements on this sample were unsuccessful. To prevent additional damage, sample V was not heated for a second time. Throughout these experiments, sample C remained intact and permissive to ultrasonic testing.

For the reasons explained above, in Table IV the shear modulus of sample V for the pre- and postwash measurements is estimated based on the relative change in the shear modulus of sample C. The same estimation is made for the longitudinal modulus of the postwash measurements. Both samples exhibited quantitatively similar relative changes of these properties during water adsorption.

2. Ultrasonic attenuation

In certain regions of p/p_0, the amplitude of measured ultrasound waves dropped precipitously, followed by recovery. In both samples, this occurred at 0.84–0.88 on adsorption and 0.88–0.75 on desorption, with the former being more prominent than the latter. During desorption, attenuation began at $p/p_0 = 0.88$, gradually increased, and peaked at 0.75, just before the pores emptied. Figure 10 exemplifies the waveforms at three distinct values of humidity. The attenuation was observed qualitatively for both longitudinal and shear waves. On desorption, at the same time as attenuation was observed, the samples became white and opaque to light.

During capillary condensation ($p/p_0 = 0.88$, adsorption) and emptying ($p/p_0 = 0.75$, desorption), the amplitude of ultrasound waves shows a significant decrease in both samples. Figure 11(a) shows the dimensionless attenuation Q^{-1} computed using the spectral ratio method [67] as a function of water saturation. The Q^{-1} is a dimensionless measure of

TABLE V. Calculated mechanical properties of sample C from ultrasound speed measurements after following the procedure outlined in the main text. The K_s is calculated using the modified Kuster-Toksöz theory outlined in the Appendix and K_f is calculated using Eq. (4), with the respective dry and solid moduli.

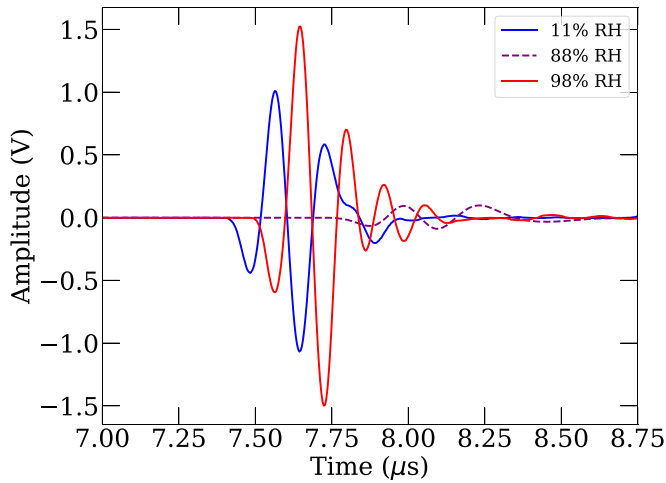| Sample condition	M_0 (GPa)	G_0 (GPa)	K_0 (GPa)	ν_0	K_s (GPa)	K_f (GPa)
12% RH	16.82	6.42	8.25	0.191	18.24	4.074
prewash, ambient	16.92	6.34	8.46	0.200	19.13	3.621
prewash, 200 °C	18.05	6.89	8.87	0.192	19.79	3.127
postwash, ambient	16.93	6.35	8.47	0.200	19.13	3.616
postwash, 200 °C	18.24	6.84	9.11	0.200	19.13	3.116

FIG. 10. Longitudinal waves produced by longitudinal transducers recorded through sample V at three humidities during adsorption, illustrating the change in travel time and the observed attenuation. The wave which exhibits maximum attenuation is drawn in dashed lines. Note that the amplitude of the 98% wave is greater than that of the 11% wave.

attenuation commonly used in the theory of viscoelasticity and geophysics and corresponds to the energy loss per one wave period (as opposed to dimensional measures such as the attenuation coefficient, which represents energy loss per meter) [68–70]. On adsorption, Q^{-1} shows a sharp peak around water saturation of 90%. This behavior of attenuation is similar to that during hexane adsorption in Vycor glass [21]. While water and hexane are significantly different fluids, the results of this work are qualitatively similar to those observed by Page *et al.* and it is reasonable to consider that the causes are the same as well. Moreover, this behavior is very similar to the behavior of elastic-wave attenuation in macroporous media partially saturated with water [71] at relatively low frequencies. This attenuation is usually attributed to the relaxation of fluid pressure between portions of the sample with different levels of liquid saturation [72] and indicates that, even on adsorption, the saturation within the sample shows slight spatial variations. These variations cause spatial variations in compressibility and thus also variations in fluid pressure in the passing wave. Fluid pressure gradients in turn cause local fluid flow through pore channels, resulting in viscous dissipation [59,72–74]. Note that this behavior of attenuation is also consistent with the behavior of the bulk modulus during adsorption [Fig. 11(b)]: K is almost constant until the liquid saturation reaches about 80%, but then increases sharply to the value given by Gassmann's equation. In a remarkable similarity to macroporous media (see [71], Fig. 1), this increase is quite sharp, but not instant.

This behavior of both bulk modulus and attenuation is characteristic of near-uniform liquid saturation, which is attained when the characteristic linear scale of saturation heterogeneity is smaller than the so-called fluid diffusion length $l_{\mathrm{d}} = (K_{\mathrm{f}}\kappa/2\pi f\eta\phi)^{1/2}$, where κ is the hydraulic permeability of the sample and η the dynamic viscosity of the fluid (see [59], Chap. 4, and references therein). Hydraulic permeability scales with the pore size squared and for a carbonate rock

corresponding to Figs. 1 and 2 of [71] is on the order of 10^{-13} m^2, which for $f = 10^3$ Hz gives l_{d} on the order of 1 cm, that is, the length scale of fluid saturation patches is below 1 cm. In contrast, due its nanoporous structure, the Vycor glass has a permeability of 5×10^{-20} m^2 [58], which for $f = 5 \times 10^6$ Hz gives l_{d} of about 100 nm. The behavior of both bulk modulus and attenuation corresponding to near-uniform saturation indicates that the water saturation on adsorption is slightly heterogeneous on the length scale below 100 nm, or several pore sizes, but is uniform on larger scales (consistent with the fact that, on adsorption, the samples remain optically transparent for the entire range of vapor pressures). The sharp attenuation peak at the saturation of 90% suggests that this attenuation only occurs when some portions of the pore space experience capillary condensation. This sharply increases the stiffness of these portions of the sample, and hence the contrast in elastic moduli between adjacent areas (some of which are still saturated only partially), which is essential for such attenuation to occur (see [59], Chaps. 3 and 4).

On desorption, both the bulk modulus and attenuation shown in Fig. 11 exhibit much more gradual saturation dependence, which is typical of so-called patchy saturation, where the scale of saturation heterogeneity is larger than l_{d}. This is consistent with the observed change in the optical properties of both samples during desorption when the hysteresis loop closed ($p/p_0 = 0.58$). At this point, the samples became white and opaque starting from the outer edge and spreading towards the center. The opacity reverted to translucency with the same radial progression between $p/p_0 = 0.58$ and $p/p_0 = 0.53$. This phenomenon was also observed by Page *et al.*, who used light scattering measurements to show the formation of large-scale inhomogeneities in the pore network as the fluid drains. These inhomogeneities are large enough to scatter light, causing the samples to become opaque. The different saturation regions permit different ultrasound speeds, which arrive out of phase at the receiving transducer to affect the shape and apparent travel time of measured ultrasonic waves. This both contributes to attenuation and causes a dip in v_{L} just as the hysteresis loop is closing.

3. Sample-transducer assembly

Figure 12 shows the photo of the sample holder used in the experiments. The transducer surface is covered by a layer of nitrile, which acts as a couplant. The sample is held between the transducers by two three-dimensionally printed plates of extruded polyethylene terephthalate glycol. The plate on the left is fixed in place. The plate on the right is movable. By rotating the wingnuts, pressure is applied to the sample via springs to ensure coupling across the transducer-sample interfaces.

Between the lowest and the highest humidities considered in this work, we observed a 14% increase in the mass of the nitrile couplant due to water absorption. Despite this, there was no effect on the travel time of ultrasonic waves through the couplant alone because its thickness was more than three times smaller than the wavelength (approximately 0.6 mm) of ultrasonic waves. Further, since the length of the couplant is three orders of magnitude less than that of the sample, any
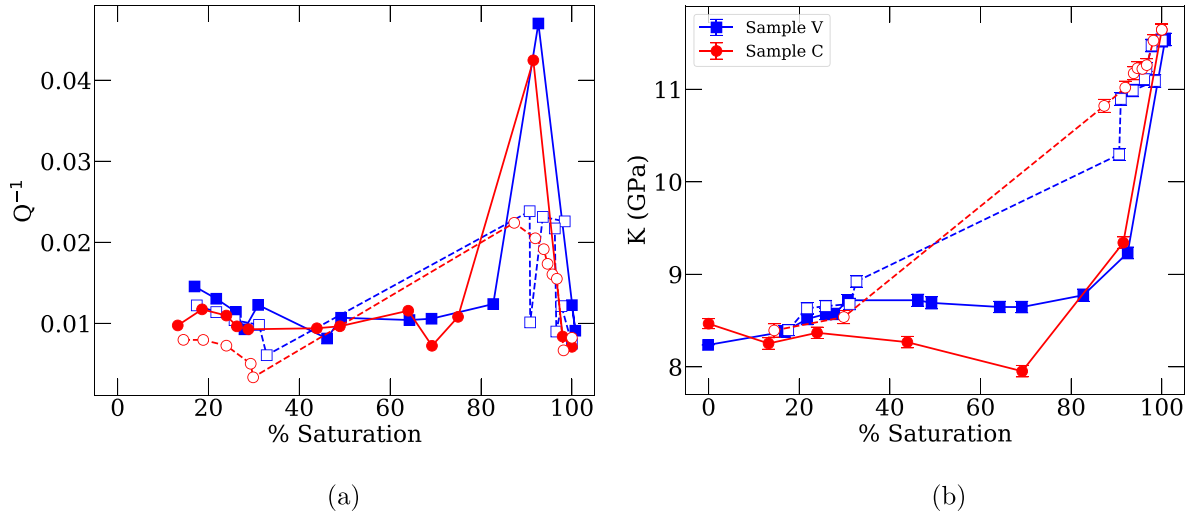
FIG. 11. (a) Attenuation of longitudinal waves through samples V (blue) and C (red) at different levels of saturation. (b) Bulk modulus of samples V and C calculated by Eq. (2) as a function of the sample saturation. Closed markers represent data on the adsorption branch, while open markers represent desorption. The error bars are propagated from the uncertainty in the longitudinal and shear moduli.

swelling upon humidification had a negligible effect on the overall travel time of ultrasonic waves.

4. Potassium acetate desiccant

The results listed in this work do not include the measurements where relative humidity was controlled by potassium acetate, used recently by Yurikov *et al.* [48] for studies of water adsorption on a sandstone sample. In solution, this salt hydrolyzes into acetic acid, which is volatile and readily releases into the air in the chamber, thus affecting the accuracy of the humidity sensor. It may also compete with water vapor for adsorption in nanopores, thus contaminating the sample. The expected RH of air above potassium acetate is 23%–26%. In practice, the reading on the RH probe approached the expected value (from room humidity, approximately 30%–40%), before parabolically increasing to approximately 75%. After opening the chamber to ambient air, the reading increased to nearly 100% and slowly returned to normal over the course of 1 h. Potassium acetate was tested again without any samples in the chamber, producing the same result described above. After purging with air, the probe reported the

correct humidities for all other salts. Subsequent ultrasound measurements with previous salts showed no difference before and after the use of potassium acetate, suggesting that any contamination was minimal or was undone by subsequent water adsorption and desorption. Because of the unreliability of the probe with this desiccant and to prevent this effect from influencing water adsorption, potassium acetate was excluded from the experiments.

5. Estimation of K_s and G_s

The bulk and shear moduli of the solid glass matrix (K_s and G_s, respectively) were estimated using the modified KT theory. The results for K_s are shown in Tables III–V. Assuming that the samples have empty cylindrical inclusions of volume fraction ϕ, the moduli of the solid phase can be calculated from the experimentally measured bulk and shear moduli of the dry samples (K_0 and G_0, respectively) using the equations

$$(K_s - K_0)\frac{K_s + \frac{4}{3}G_s}{K_0 + \frac{4}{3}G_s} = \phi K_s P^{sp}, \tag{A1}$$

$$(G_s - G_0)\frac{G_s + F_s}{G_0 + F_s} = \phi G_s Q^{sp}, \tag{A2}$$

where

$$F_s = \frac{G_s}{6}\frac{9K_s + 8G_s}{K_s + 2G_s}, \tag{A3}$$

$$P^{sp} = \frac{K_s + G_s}{G_s}, \tag{A4}$$

$$P^{sp} = \frac{1}{5}\left(\frac{16}{3} + 2\frac{G_s + \gamma_s}{\gamma_s}\right), \tag{A5}$$

and

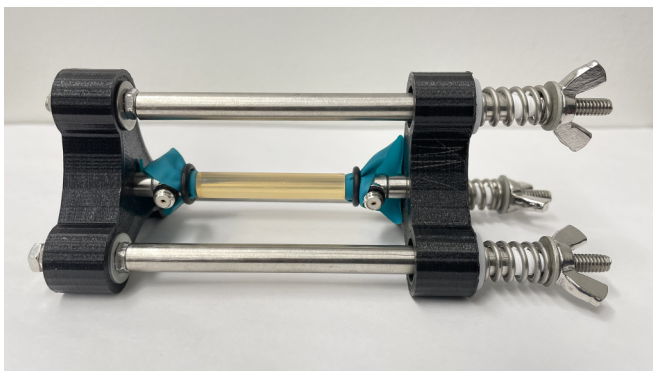$$\gamma_s = G_s\frac{3K_s + G_s}{3K_s + 7G_s}. \tag{A6}$$

FIG. 12. Photo of the assembly used to measure the sound speed of the glass samples.

[1] W. Thomson, On the equilibrium of vapour at a curved surface of liquid, Proc. R. Soc. Edinburgh **7**, 63 (1872).

[2] V. Karasev, B. Derjaguin, and E. Khromova, *Collection Researches in Surface Forces* (Consultants Bureau, New York, 1971), Vol. 3, pp. 25–28.

[3] B. Derjaguin, V. Karasev, and E. Khromova, Thermal expansion of water in fine pores, J. Colloid Interface Sci. **109**, 586 (1986).

[4] P. Huber, Soft matter in hard confinement: Phase transition thermodynamics, structure, texture, diffusion and flow in nanoporous media (topical review), J. Phys.: Condens. Matter **27**, 103102 (2015).

[5] K. E. Gubbins, Y. Long, and M. Śliwinska-Bartkowiak, Thermodynamics of confined nano-phases, J. Chem. Thermodyn. **74**, 169 (2014).

[6] E. Barsotti, S. P. Tan, S. Saraji, M. Piri, and J.-H. Chen, A review on capillary condensation in nanoporous media: Implications for hydrocarbon recovery from tight reservoirs, Fuel **184**, 344 (2016).

[7] R. Kimmich, Strange kinetics, porous media, and NMR, Chem. Phys. **284**, 253 (2002).

[8] S. Xu, G. C. Simmons, T. Mahadevan, G. W. Scherer, S. H. Garofalini, and C. Pacheco, Transport of water in small pores, Langmuir **25**, 5084 (2009).

[9] S. Xu, G. W. Scherer, T. Mahadevan, and S. H. Garofalini, Thermal expansion of confined water, Langmuir **25**, 5076 (2009).

[10] J. J. Valenza, II and G. W. Scherer, Evidence of anomalous thermal expansion of water in cement paste, Cem. Concr. Res. **35**, 57 (2005).

[11] K. Schappert and R. Pelster, Influence of the Laplace pressure on the elasticity of argon in nanopores, Europhys. Lett. **105**, 56001 (2014).

[12] C. D. Dobrzanski, B. Gurevich, and G. Y. Gor, Elastic properties of confined fluids from molecular modeling to ultrasonic experiments on porous solids, Appl. Phys. Rev. **8**, 021317 (2021).

[13] T. M. Müller and B. Gurevich, Wave-induced fluid flow in random porous media: Attenuation and dispersion of elastic waves, J. Acoust. Soc. Am. **117**, 2732 (2005).

[14] J. J. Valenza, II, N. Drenzek, F. Marques, M. Pagels, and M. Mastalerz, Geochemical controls on shale microstructure, Geology **41**, 611 (2013).

[15] F. Gassmann, Über die elastizität poröser medien, Viertel. Naturforsch. Ges. Zürich **96**, 1 (1951).

[16] M. A. Biot, Theory of propagation of elastic waves in a fluid-saturated porous solid. I. Low-frequency range, J. Acoust. Soc. Am. **28**, 168 (1956).

[17] M. A. Biot, Theory of propagation of elastic waves in a fluid-saturated porous solid. II. Higher frequency range, J. Acoust. Soc. Am. **28**, 179 (1956).

[18] L. Pimienta, C. David, J. Sarout, X. Perrot, J. Dautriat, and C. Barnes, Evolution in seismic properties during low and intermediate water saturation: Competing mechanisms during water imbibition? Geophys. Res. Lett. **46**, 4581 (2019).

[19] S. K. Tadavani, K. M. Poduska, A. E. Malcolm, and A. Melnikov, A non-linear elastic approach to study the effect of ambient humidity on sandstone, J. Appl. Phys. **128**, 244902 (2020).

[20] K. L. Warner and J. R. Beamish, Ultrasonic measurement of the surface area of porous materials, J. Appl. Phys. **63**, 4372 (1988).

[21] J. H. Page, J. Liu, B. Abeles, E. Herbolzheimer, H. W. Deckman, and D. A. Weitz, Adsorption and desorption of a wetting fluid in Vycor studied by acoustic and optical techniques, Phys. Rev. E **52**, 2763 (1995).

[22] K. Schappert and R. Pelster, Elastic properties of liquid and solid argon in nanopores, J. Phys.: Condens. Matter **25**, 415302 (2013).

[23] K. Schappert, L. Gemmel, D. Meisberger, and R. Pelster, Elasticity and phase behaviour of *n*-heptane and *n*-nonane in nanopores, Europhys. Lett. **111**, 56003 (2015).

[24] K. Schappert and R. Pelster, Temperature dependence of the longitudinal modulus of liquid argon in nanopores, J. Phys. Chem. C **122**, 5537 (2018).

[25] K. Schappert and R. Pelster, Liquid argon in nanopores: The impact of confinement on the pressure dependence of the adiabatic longitudinal modulus, J. Phys. Chem. C **122**, 27425 (2018).

[26] K. Schappert and R. Pelster, Distinct enhancement of the longitudinal modulus of liquid nitrogen in nanoporous Vycor glass, J. Phys. Chem. C **126**, 21745 (2022).

[27] G. Y. Gor, Adsorption stress changes the elasticity of liquid argon confined in a nanopore, Langmuir **30**, 13564 (2014).

[28] Z. Sun, Y. Kang, and Y. Kang, Density functional study on enhancement of modulus of confined fluid in nanopores, Ind. Eng. Chem. Res. **58**, 15637 (2019).

[29] C. D. Dobrzanski, M. A. Maximov, and G. Y. Gor, Effect of pore geometry on the compressibility of a confined simple fluid, J. Chem. Phys. **148**, 054503 (2018).

[30] G. Y. Gor and B. Gurevich, Gassmann theory applies to nanoporous media, Geophys. Res. Lett. **45**, 146 (2018).

[31] M. A. Maximov and G. Y. Gor, Molecular simulations shed light on potential uses of ultrasound in nitrogen adsorption experiments, Langmuir **34**, 15650 (2018).

[32] C. H. Amberg and R. McIntosh, A study of adsorption hysteresis by means of length changes of a rod of porous glass, Can. J. Chem. **30**, 1012 (1952).

[33] K. Hiller, Strength reduction and length changes in porous glass caused by water vapor adsorption, J. Appl. Phys. **35**, 1622 (1964).

[34] C. Hodgson and R. McIntosh, The freezing of water and benzene in porous Vycor glass, Can. J. Chem. **38**, 958 (1960).

[35] O. Petrov and I. Furó, A study of freezing–melting hysteresis of water in different porous materials. Part I: Porous silica glasses, Microporous Mesoporous Mater. **138**, 221 (2011).

[36] S. Gruener, Z. Sadjadi, H. E. Hermes, A. V. Kityk, K. Knorr, S. U. Egelhaaf, H. Rieger, and P. Huber, Anomalous front broadening during spontaneous imbibition in a matrix with elongated pores, Proc. Natl. Acad. Sci. USA **109**, 10245 (2012).

[37] S. Kiepsch and R. Pelster, Interplay of vapor adsorption and liquid imbibition in nanoporous Vycor glass, Phys. Rev. E **93**, 043128 (2016).

[38] S. Gruener, D. Wallacher, S. Greulich, M. Busch, and P. Huber, Hydraulic transport across hydrophilic and hydrophobic nanopores: Flow experiments with water and *n*-hexane, Phys. Rev. E **93**, 013102 (2016).

[39] A. Taschin, R. Cucini, P. Bartolini, and R. Torre, Temperature of maximum density of water in hydrophilic confinement measured by transient grating spectroscopy, Europhys. Lett. **92**, 26005 (2010).

[40] M.-C. Bellissent-Funel, Structure of confined water, J. Phys.: Condens. Matter **13**, 9165 (2001).

[41] H. Thompson, A. K. Soper, M. A. Ricci, F. Bruni, and N. T. Skipper, The three-dimensional structure of water confined in nanoporous Vycor glass, J. Phys. Chem. B **111**, 5610 (2007).

[42] V. D. Borman, A. A. Belogorlov, and V. N. Tronin, Anomalously slow relaxation of interacting liquid nanoclusters confined in a porous medium, Phys. Rev. E **93**, 022142 (2016).

[43] P. Levitz, Probing interfacial dynamics of water in confined nanoporous systems by NMRD, Mol. Phys. **117**, 952 (2019).

[44] W. F. Murphy, Effects of partial water saturation on attenuation in Massilon sandstone and Vycor porous glass, J. Acoust. Soc. Am. **71**, 1458 (1982).

[45] R. Cucini, A. Taschin, P. Bartolini, and R. Torre, Acoustic, thermal and flow processes in a water filled nanoporous glass by time-resolved optical spectroscopy, J. Mech. Phys. Solids **58**, 1302 (2010).

[46] P. I. Ravikovitch and A. V. Neimark, Characterization of nanoporous materials from adsorption and desorption isotherms, Colloids Surf. A **187–188**, 11 (2001).

[47] M. Thommes, B. Smarsly, M. Groenewolt, P. I. Ravikovitch, and A. V. Neimark, Adsorption hysteresis of nitrogen and argon in pore networks and characterization of novel micro- and mesoporous silicas, Langmuir **22**, 756 (2006).

[48] A. Yurikov, M. Lebedev, G. Y. Gor, and B. Gurevich, Sorption-induced deformation and elastic weakening of Bentheim sandstone, J. Geophys. Res. Solid Earth **123**, 8589 (2018).

[49] R. Weast, *CRC Handbook of Chemistry and Physics 1976-1977: A Ready-Reference Book of Chemical and Physical Data*, 57th ed. (CRC, Boca Raton, 1976).

[50] R. G. Lyons, *Understanding Digital Signal Processing*, 3rd ed. (Pearson Education Canada, North York, 2010).

[51] G. T. Kuster and M. N. Toksöz, Velocity and attenuation of seismic waves in two-phase media: Part I. Theoretical formulations, Geophysics **39**, 587 (1974).

[52] J. G. Berryman, Long-wavelength propagation in composite elastic media II. Ellipsoidal inclusions, J. Acoust. Soc. Am. **68**, 1820 (1980).

[53] Y. Sun, B. Gurevich, and G. Y. Gor, Modeling elastic properties of Vycor glass saturated with liquid and solid adsorbates, Adsorption **25**, 973 (2019).

[54] G. W. Scherer, Dilatation of porous glass, J. Am. Ceram. Soc. **69**, 473 (1986).

[55] N. Markova, E. Sparr, and L. Wadso, On application of an isothermal sorption microcalorimeter, Thermochim. Acta **374**, 93 (2001).

[56] I. H. Bell, J. Wronski, S. Quoilin, and V. Lemort, Pure and Pseudo-pure fluid thermophysical property evaluation and the Open-Source Thermophysical Property Library CoolProp, Ind. Eng. Chem. Res. **53**, 2498 (2014).

[57] W. Wagner and A. Pruß, The IAPWS formulation 1995 for the thermodynamic properties of ordinary water substance for general and scientific use, J. Phys. Chem. Ref. Data **31**, 387 (2002).

[58] W. Vichit-Vadakan and G. W. Scherer, Measuring permeability of rigid materials by a beam-bending method: II, Porous glass, J. Am. Ceram. Soc. **83**, 2240 (2000).

[59] B. Gurevich and J. M. Carcione, *Attenuation and Dispersion of Elastic Waves in Porous Rocks: Mechanisms and Models* (Society of Exploration Geophysicists, Houston, 2022).

[60] G. Mavko and D. Jizba, Estimating grain-scale fluid effects on velocity dispersion in rocks, Geophysics **56**, 1940 (1991).

[61] G. Y. Gor and A. V. Neimark, Adsorption-induced deformation of mesoporous solids, Langmuir **26**, 13021 (2010).

[62] F. D. Murnaghan, The compressibility of media under extreme pressures, Proc. Natl. Acad. Sci. USA **30**, 244 (1944).

[63] F. Birch, Elasticity and constitution of the Earth's interior, J. Geophys. Res. **57**, 227 (1952).

[64] G. Y. Gor, D. W. Siderius, C. J. Rasmussen, W. P. Krekelberg, V. K. Shen, and N. Bernstein, Relation between pore size and the compressibility of a confined fluid, J. Chem. Phys. **143**, 194506 (2015).

[65] G. Y. Gor, D. W. Siderius, V. K. Shen, and N. Bernstein, Modulus–pressure equation for confined fluids, J. Chem. Phys. **145**, 164505 (2016).

[66] See Supplemental Material at http://link.aps.org/supplemental/10.1103/PhysRevE.108.024802 for the data shown in the figures.

[67] F. M. Sears and B. P. Bonner, Ultrasonic attenuation measurement by spectral ratios utilizing signal processing techniques, IEEE Trans. Geosci. Remote **GE-19**, 95 (1981).

[68] L. Knopoff, Q, Rev. Geophys. **2**, 625 (1964).

[69] K. W. Winkler and T. J. Plona, Technique for measuring ultrasonic velocity and attenuation spectra in rocks under pressure, J. Geophys. Res. Solid Earth **87**, 10776 (1982).

[70] C. McCann and J. Sothcott, Sonic to ultrasonic Q of sandstones and limestones: Laboratory measurements at *in situ* pressures, Geophysics **74**, WA93 (2009).

[71] T. Cadoret, G. Mavko, and B. Zinszner, Fluid distribution effect on sonic attenuation in partially saturated limestones, Geophysics **63**, 154 (1998).

[72] Y. Kobayashi and G. Mavko, Variation in P-wave modulus with frequency and water saturation: Extension of dynamic-equivalent-medium approach, Geophysics **81**, D479 (2016).

[73] J. E. White, Computed seismic speeds and attenuation in rocks with partial gas saturation, Geophysics **40**, 224 (1975).

[74] D. L. Johnson, Theory of frequency dependent acoustics in patchy-saturated porous media, J. Acoust. Soc. Am. **110**, 682 (2001).